

## ARTICLE OPEN



## Curved digital X-ray detectors

Albert J.J.M. van Breemen<sup>1</sup>, Matthias Simon<sup>2</sup>, Olivier Tousignant<sup>3,6</sup>, Santhosh Shanmugam<sup>1</sup>, Jan-Laurens van der Steen<sup>1</sup>, Hylke B. Akkerman<sup>1</sup>, Auke Kronemeijer<sup>1</sup>, Walter Ruetten<sup>2</sup>, Rob Raaijmakers<sup>3,7</sup>, Lex Alving<sup>3</sup>, Jan Jacobs<sup>3</sup>, Pawel E. Malinowski<sup>4</sup>, Florian De Roose<sup>4</sup> and Gerwin H. Gelinck<sup>1,5</sup>✉

A curved image sensor on plastic foil has been developed for cone beam computed tomography (CBCT) X-ray imaging. The image sensor of about  $6 \times 8 \text{ cm}^2$  size has been built on a thin polyimide foil with an indium gallium zinc oxide (IGZO) backplane and an organic photodetectors (OPD) frontplane. A flexible cesium iodide (CsI) scintillator has been attached to the optical sensor with  $480 \times 640$  pixels of  $126 \mu\text{m}$  size. Dark current density of the OPD was low with less than  $10^{-7} \text{ mA/cm}^2$  at  $-2 \text{ V}$ , while an external quantum efficiency (EQE) of about 50% was reached in the visible wavelength range matched to the scintillator output. The image quality of the digital X-ray detector allowed for 3D reconstruction images of a bone phantom on a rotating stage with a lab setup. The curved detector with 32 cm curvature radius opens up the path for very compact CBCT gantries with largely reduced footprint.

npj Flexible Electronics (2020)4:22; <https://doi.org/10.1038/s41528-020-00084-7>

## INTRODUCTION

Curved surfaces are the preferred shape for image sensors—just think of the human eyeball and the 35 mm photographic plastic film used in analog photocopier. Nevertheless, today's digital image sensor arrays are flat and suffer from vignetting, i.e., image quality decreases from the center to the edge of the detector due to the angle at which the photons hit the outer pixels. Vignetting is typically combatted with a series of optical lenses, but that results in a bulky optical system. Curved and hemispherical detectors would not need such lenses, thereby simplifying the optical lens system ultimately to a simple, one-lens configuration<sup>1</sup>. Previous curved image sensor prototypes have been made on thinned glass or silicon substrate<sup>2–4</sup>. This typically results in fragile imagers that are typically transferred to a plastic or rubber supporting substrate. Hemispherical electronic eye cameras made from ultra-thin single-crystalline silicon have been transferred to rubber substrates using a lamination procedure<sup>5</sup>. By pre-stretching the rubber, small-area arrays of photodetectors in distinct, three-dimensional geometries have been realized<sup>6</sup>. Two-dimensional semiconductor/semimetal materials like  $\text{MoS}_2$  and graphene on strategically configured supporting polymer foils enabled a low resolution 3D photodetection and imaging system capable of sensing both the direction and intensity of illumination. Fan et al.<sup>7</sup> demonstrated a curved photodiode array using a thin, flexible polyimide foil substrate. An  $8 \times 100$  array of thin-film InGaAs p–i–n photodiodes was realized on a conventional (growth) InP substrate, and subsequently bonded to the polyimide substrate via cold-weld bonding and finally released from the growth substrate, yielding a convex cylindrically curved imager with a  $360^\circ$  field of view. In all the above work, the pixels are rather large, and the total array area rather small.

Here, we report a high-resolution curved image sensor made directly on a thin plastic substrate using organic photodetectors (OPD). The use of OPD offers a number of advantages over their inorganic counterparts. They can be processed over large area from solution using low process temperatures. These advantages allow monolithic fabrication of large-area photodetector arrays on

plastic substrates, using process steps that are compatible with existing manufacturing methods to make flexible displays. The OPD are coated on a 200-ppi amorphous indium gallium zinc oxide (IGZO) TFT backplane. As a proof-of-concept, the curved digital detector (radius of curvature 32 cm) was combined with a flexible scintillator and integrated into a demonstration cone beam computed tomography (CBCT) X-ray system<sup>8,9</sup> (Fig. 1). Such compact systems with a curved detector have been investigated by simulations, but up to now never realized yet, to our knowledge<sup>10</sup>. The curved detector's more uniform image quality combined with 3D reconstruction algorithms yielded better 3D views compared to the flat digital detector. In addition, the volume of 3D X-ray imaging systems was shrunk by 50% (Fig. S2).

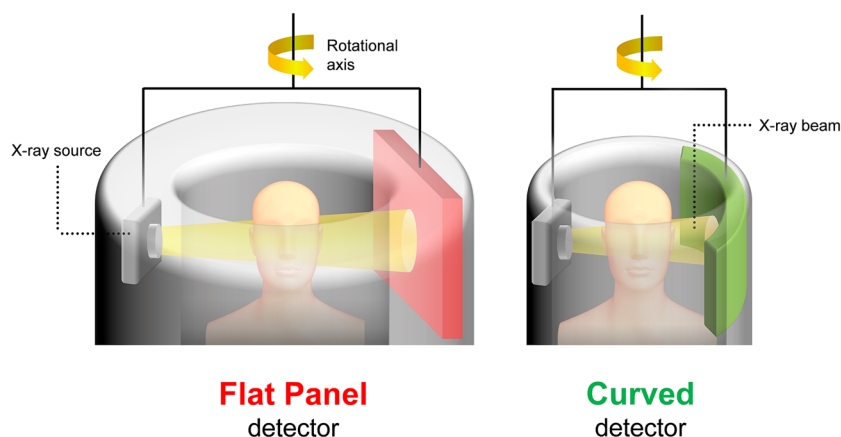
## RESULTS

Figure 2a shows the cross section of the digital X-ray detector-on-foil. It consists of (1) an IGZO-based active-matrix TFT backplane fabricated on a polyimide foil, followed by (2) an inverted stack OPD frontplane that is formed by a  $\sim 300 \text{ nm}$  thick photoactive organic layer sandwiched between bottom pixel electrode and non-patterned optically transparent top electrode, (3) an optically transparent thin-film barrier, and finished by (4) a bendable CsI scintillator, developed by Hamamatsu Photonics (Japan).

The IGZO TFT backplane is processed on a  $\text{SiN}_x$  bottom encapsulation barrier on polyimide foil/glass carrier via a series of lithographic mask steps. The display-compatible TFT fabrication process is discussed in detail both previously<sup>11</sup> and in the "Methods". Transfer characteristics of 25 transistors with a channel length of  $20 \mu\text{m}$  and a channel width of  $60 \mu\text{m}$  equally distributed over the  $320 \times 352 \text{ mm}$  substrate are presented in Fig. 3a. The TFTs show a typical mobility of  $15.1 \pm 0.8 \text{ cm}^2/\text{Vs}$ , onset voltage ( $V_{\text{ON}}$ ) of  $0.4 \pm 0.3 \text{ V}$ , ON/OFF-current ratio  $\sim 10^7$ , and a subthreshold swing of  $0.4 \pm 0.02 \text{ V/decade}$ .

In the current digital detector, we employed a single pass transistor configuration per pixel, as used in most current X-ray imaging products. The TFT switch requires a high ON/OFF ratio, a reasonably sharp turn-ON region but particularly a low leakage.

<sup>1</sup>Holst Centre/TNO, Eindhoven, The Netherlands. <sup>2</sup>Philips Research, Eindhoven, The Netherlands. <sup>3</sup>Philips Healthcare, Best, The Netherlands. <sup>4</sup>imec, Leuven, Belgium. <sup>5</sup>Department of Applied Physics, Technical University Eindhoven, Eindhoven, The Netherlands. <sup>6</sup>Present address: Teledyne Dalsa, Eindhoven, The Netherlands. <sup>7</sup>Deceased: Rob Raaijmakers. ✉email: Gerwin.gelinck@tno.nl



**Fig. 1 Curved vs. planar flat panel digital X-ray detector in medical cone beam computed tomography (CBCT).** CBCT is a technology that creates three-dimensional views of objects based on a series of two-dimensional X-ray images. Today's CBCT systems are typically very large as they have a 2D flat panel digital X-ray detector mounted on a gantry that rotates around the subject being examined to capture the data required for a 3D image reconstruction. Here, curving the detector would mean its edges describe a smaller circle as the gantry rotates, so the whole system could be more compact. See Supplementary Information for more details. A planar X-ray source is shown instead of a bulky X-ray source for the sake of simplicity.

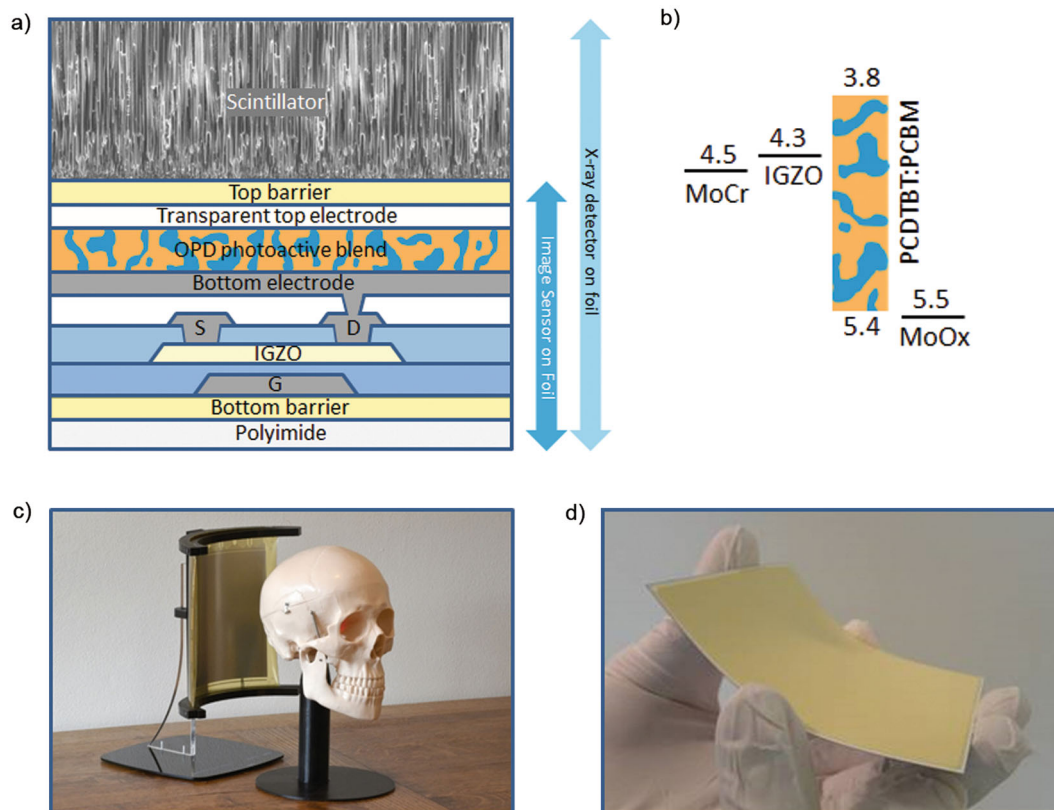


**Fig. 2 Digital X-ray detector-on-foil.** **a** Cross section of the digital X-ray detector-on-foil. A solution-processed BHJ organic photodetector frontplane with p-type polymer donor (orange) and small molecule n-type acceptor (blue) is integrated on top of an IGZO TFT backplane. **b** Band diagram of the OPD frontplane. For the OPD active blend, only the energy levels of the HOMO of PCDTBT (5.4 eV) and LUMO of PCBM (3.8 eV) are shown. **c** Prototype of curved image sensor. **d** Bendable Hamamatsu FSS 600 CsI scintillator.

The low OFF-current of substantially  $<1$  pA compares favorably to amorphous and polycrystalline silicon transistors. This is inherent to IGZO as the low leakage current is related to the large bandgap of IGZO ( $\sim 3$  eV). The formation of the OPD on top of the IGZO transistor does not affect the IGZO TFT properties. This is also not expected as the OPD deposition occurs at much lower temperatures than the maximum process temperature during IGZO TFT fabrication.

The photodetector is based on a bulk heterojunction (BHJ) structure, with a donor polymer and an acceptor fullerene derivative. BHJ photodetectors show high photogeneration sensitivities, fast response times, and their absorption can be tuned from the ultraviolet to the near-infrared<sup>12,13</sup>. Moreover, they can be solution-processed at low temperatures and on flexible substrates by roll-to-roll and sheet-to-sheet large-area processing techniques<sup>14,15</sup>. In this work, we have used a 280 nm thick blend

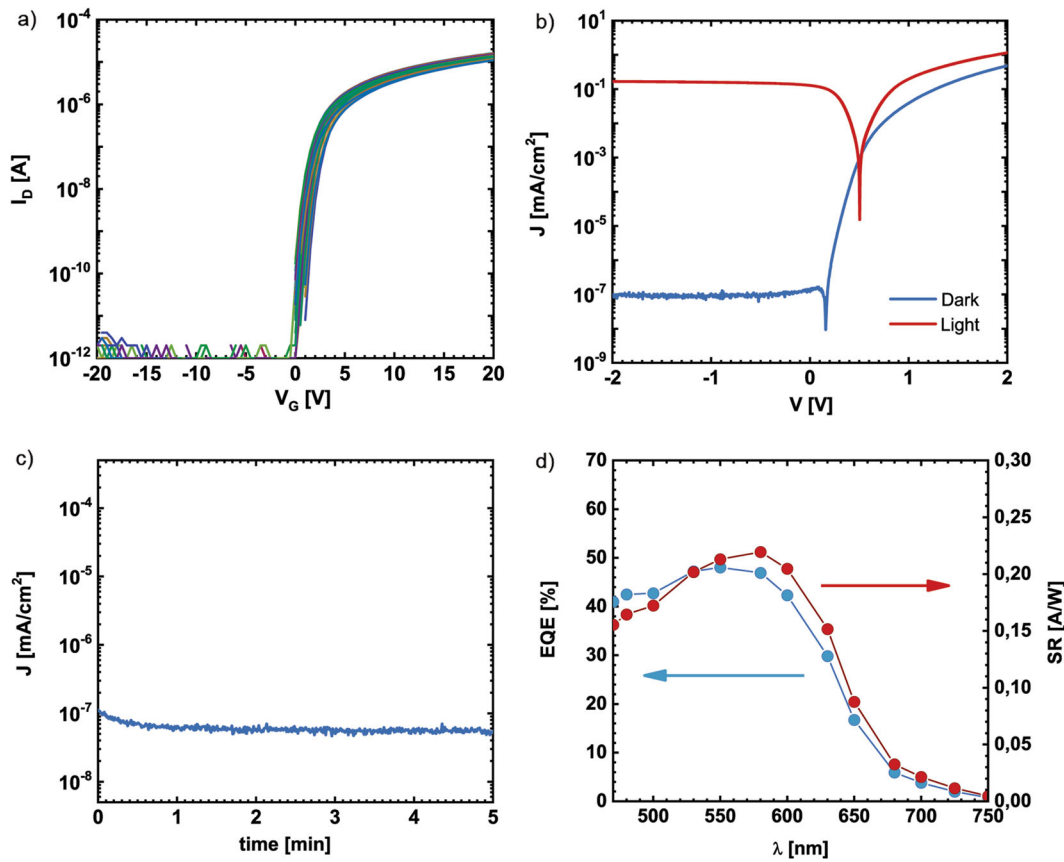


**Fig. 3** Characteristics of discrete IGZO TFTs and OPDs. **a** Transfer characteristics of 25 IGZO TFTs ( $W/L$  60/20  $\mu\text{m}$ ) distributed over a GEN1 substrate ( $320 \times 352$  mm), measured at a source–drain voltage of 1 V. **b** Current density of OPD as a function of voltage under dark (blue) and low light intensity (red) conditions (light intensity of ca. 0.1  $\text{mW}/\text{cm}^2$ ). **c** Current density of OPD as a function of time measured at  $-2$  V under dark conditions. **d** EQE (blue) and spectral response (red) of OPD as a function of wavelength.

of poly[N-9'-heptadecanyl-2,7-carbazole-alt-5,5-(4',7'-di-2-thienyl-2',1',3'-benzothiadiazole)], PCDTBT, a p-type (donor) polymer<sup>16,17</sup> and [6,6]-phenyl-C61-butyric acid methyl ester, PCBM, (acceptor) fullerene<sup>18</sup>, followed by a thermally evaporated  $\text{MoO}_x$  hole transport layer and a thin Ag semitransparent anode. Finally, a top transparent thin-film encapsulation barrier<sup>19</sup> is processed (Fig. 2b). Figure 2c, d show photographs of curved image sensor and flexible scintillator, respectively. Details of the step by step fabrication can be found in the “Experimental” section.

OPD test devices having the same layer stack as the OPD frontplane and processed in the same way were also fabricated. These devices were used to measure the OPD performance and consisted of a series of 1  $\text{mm}^2$  pixels. Figure 3b shows the current density–voltage ( $J$ – $V$ ) characteristics of the OPDs in dark ( $J_d$ ) and under illumination of low intensity, white light ( $J_{\text{photo}}$ ). The nonzero  $J_d$  at 0 V results from transient displacement currents that occur during a  $J$ – $V$  sweep even at very low scan rates. We consider the static measurement to be a more reliable way of determining  $J_d$ . Figure 3c depicts a static measurement of  $J_d$  at  $-2$  V over a time interval of 5 min. Typically, the OPDs have a leakage current density of  $0.3\text{--}1 \times 10^{-7}$   $\text{mA}/\text{cm}^2$  at  $-2$  V (Supplementary Fig. 3). This value is lower than that of low-temperature a-Si PDs<sup>20,21</sup> ( $10^{-6}$ – $10^{-7}$   $\text{mA}/\text{cm}^2$ ) and on par to the  $10^{-7}$   $\text{mA}/\text{cm}^2$  value reported for high-temperature a-Si p–i–n photodiodes<sup>20</sup>. It compares favorably with other reported dark current densities for BHJ based OPDs with  $\sim 300$  nm thick active layers<sup>22,23</sup>. For an OPD pixel of  $126 \times 126 \mu\text{m}^2$  with a fill factor of 50% this would translate to a leakage current of  $8 \times 10^{-15}$  A. The leakage current of the TFT used in the curved detector ( $W = 60 \mu\text{m}$ ) is below  $6 \times 10^{-15}$  A, hence even lower than that of the OPD. The leakage current of the

TFT is estimated from TFT measurements on devices with larger channel widths. It can be seen that  $J_{\text{photo}}$  is orders of magnitude larger than  $J_d$ . We found  $V_{\text{oc}}$  to decrease reciprocally with  $\ln(I)$  with the light intensity. The so-called ideality factor  $n$  was 1.6.  $V_{\text{oc}}$  was determined to be 0.85 V under simulated solar light (AM1.5G, 100  $\text{mW}/\text{cm}^2$ ).

The external quantum efficiency (EQE) and spectral responsivity (SR) vs. wavelength at a reverse bias of  $-2$  V are depicted in Fig. 3d. Both metrics peak near the emission wavelength of the CsI:Tl scintillator of 550 nm used in this work ([https://www.hamamatsu.com/resources/pdf/ssd/e09\\_handbook\\_xray\\_detectors.pdf](https://www.hamamatsu.com/resources/pdf/ssd/e09_handbook_xray_detectors.pdf)) at values of 48% and 0.21 A/W, respectively. Simulations show that a photodiode quantum efficiency of 48% with a dark current density lower than  $10^{-6}$   $\text{mA}/\text{cm}^2$  image quality is determined by the random variations in the number of X-ray photons that are generated and absorbed by the scintillator<sup>24</sup>. The noise current density,  $I_N$ , was measured at reverse bias between 1 and 50 Hz (Supplementary Fig. 4). Below ca. 10 Hz a  $1/f$  behavior is observed. Above 10 Hz, the frequency response was flat, at  $\approx 8$  fA  $\text{Hz}^{1/2}$ . Taking this value together with SR of 0.21 A/W, the specific detectivities  $D^* = \text{SR} \sqrt{A}/I_N$  (in Jones, where Jones =  $\text{cm}^2 \text{Hz}^{1/2}/\text{W}$  and A is device area). At  $-2$  V bias, the calculated maximum specific detectivity  $D^* = 3 \times 10^{12}$  Jones (at  $\sim 550$  nm). With a dark current density as low as  $3 \times 10^{-8}$   $\text{mA}/\text{cm}^2$ , sensitivity of 0.21 A/W, and specific detectivity of  $3 \times 10^{12}$  Jones in the green wavelength range, the performance of our solution-processed photodetector rank amongst the best so far for OPDs<sup>11,22,23</sup>.

A sensor array of  $480 \times 640$  pixels,  $126 \times 126 \mu\text{m}^2$  in size, is built. The photodiodes are operated with a reverse bias voltage, of typically a few Volt. The positive electrodes of the photodiodes are

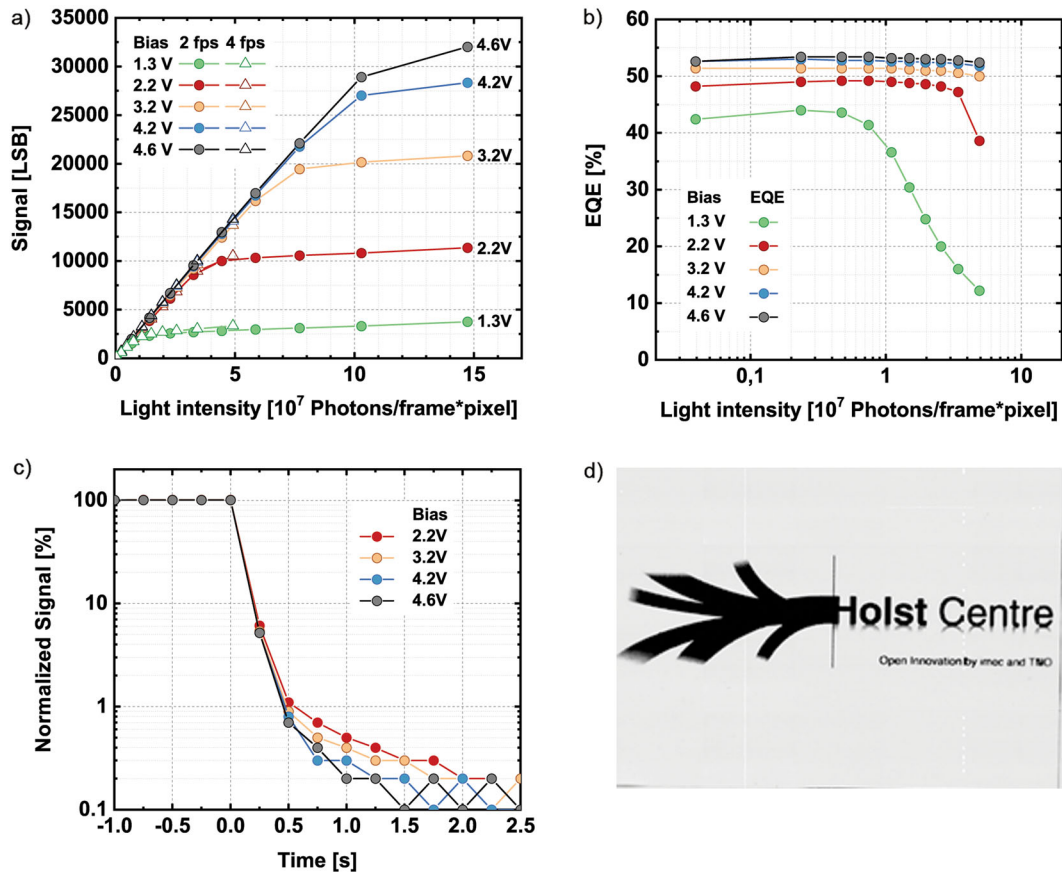


**Fig. 4 Optical array characteristics.** **a** Light signal in least significant bits (LSB, ADC digital output) vs. impinging light intensity. Photons per frame and pixel are varied via length of the light pulse and calculated from the measured light power per  $\text{cm}^2$ . The applied photodiode bias voltage was varied. The measurement was done for 2 frames per second (fps), equivalent to 500 ms integration time and 4 fps, equivalent to 250 ms integration time. A log–log plot of (a) is shown in Supplementary Fig. 5. **b** EQE as calculated from the slope of the graphs from (a) vs. impinging light intensity. **c** Temporal behavior of the image sensor. At  $t = 0$  the light pulse is switched off, and the decay of photocurrent is monitored for different applied biases. **d** Optical image taken with the image sensor on foil.

formed by the optically transparent common electrode (Fig. 2a). The negative, patterned, and bottom electrodes of the photodiodes of a column are connected to the data line via a TFT. The gates of the TFTs of a row are connected to a common gate line. The flat panel sensor is scanned one-row-at-a-time by a dedicated row driver, in a similar way as active-matrix displays. During one frame time all the rows are sequentially selected and TFTs switch from the non-conducting to the conducting (“ON”) state. With the TFTs in the ON state charge sense amplifiers (CSAs) coupled to the data line detect the pixel current as the TFT transfers the charge from the photodiode capacitance to the data line until the voltage across the photodiode is back to its original value. Current levels are digitized using analog-to-digital converters (ADCs). More details can be found here in ref. <sup>11</sup>.

In order to characterize the optical response, we illuminate the OPD arrays from the top, using a large-area homogenous LED light source. The mean wavelength of 540 nm is similar to the light produced by a typical CsI-Tl based X-ray scintillator.

Figure 4a shows the spatially averaged image sensor signal of all pixels in the array as a function of light intensity for different reverse bias voltage over the photodiode and two image scan rates, 2 and 4 frames per second (fps). The average light intensity is changed by keeping the driving current of the LED light source constant, and varying the pulse length from 1 ms to the maximum possible length determined by the integration time of the sensor, which is the inverse of the repetition rate (frame rate) of the sensor readout. Light intensity is measured at the position of the sensor array with a light power meter (Advantest TQ9210). With

known wavelength and pulse duration the power is converted into the number of impinging optical photons per integration time. The output of the ADC in the unit least significant bit (LSB) can be converted to electrical charge with the known sensitivity of the amplifier of  $900 \text{ e}^-/\text{LSB}$ .

The output signal does not depend on the frame rate of the image sensor. The signal increases linearly with light intensity before a plateau is reached indicating saturation of the photodiode capacity. From the readout charge at the plateau values the capacity of the photodiode ( $C = Q/V$ ) is calculated to be 1.4 pF. This is well in line with the geometrical capacitance of 1.5 pF calculated for a capacitor with an area of  $126 \times 126 \mu\text{m}^2$ , OPD layer thickness of 285 nm and estimated dielectric constant of 3. From the slope of the curves in Fig. 4a (log–log plot is shown in Supplementary Fig. 5) the sensitivity of the sensor and thus the EQE can be deduced. In Fig. 4b the EQE is plotted vs. light intensity using the data of Fig. 4a (4 fps frame rate only). For a bias voltage of 4.6 V the EQE is about 53%. For a wavelength of 550 nm the spectral sensitivity is  $R = 0.24 \text{ A/W}$ . With decreasing bias the EQE decreases slightly, to 42% for a bias voltage of 1.3 V. These values are in good agreement with the results of single photodiodes (Fig. 3). The sudden drop in EQE at high light intensities for voltages of 1.3 and 2.2 V in the sensor array originates from saturation of the pixel capacitance.

The temporal response of the sensor array is measured by a sequence of illuminated images followed by images where the light source is switched off. As shown in Fig. 4c there is still some charge detected in the non-illuminated images, a phenomenon



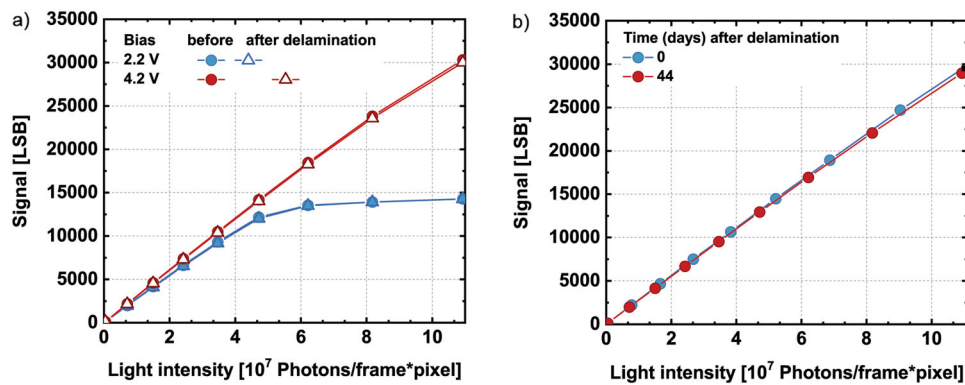


**Fig. 5 Flexible array characteristics.** **a** Light response (least significant bits, LSB) vs. impinging light intensity for the image sensor on foil still on the glass carrier (closed symbols) and after delamination (open symbols) for two different photodiode bias voltages. **b** Long-term stability of image sensor on foil just after delamination (black,  $t = 0$ ), and after 44 days ( $t = 44$ ) in ambient.

known as residual signal or lag also from other noncrystalline photodiodes like a-Si<sup>25</sup>. The residual signal is attributed to charges in the photodiode, which are released from deep traps after a certain time<sup>26</sup>. The residual signal is in the order of a few tenths of a percent of the signal height during illumination 1 s after end of the illumination. It is decreasing with increasing bias voltage due to faster removal of charge with higher bias field. After about 2 s the residual signal falls below our measurement limit of about 0.2%. The temporal response is comparable to standard a-Si X-ray digital detectors and thus good enough for the initial medical application. The impact of lag or “residual signal” depends not only on the frame rate, but also on the medical application. For long-term low dose X-ray video imaging (fluoroscopy) applications, a-Si-based X-ray detectors are frequently used without problems with 30–60 fps frame rate. For 3D imaging (cone beam CT) with C-arm systems they are used normally up to 30 fps, too. Here the residual signal can produce some artefacts (rings) after 3D image reconstruction, which have to be corrected by software.

An optical image is taken with a b/w photograph printed on a transparent slide on top of the sensor array (Fig. 4d). For this image a dark image is subtracted (offset correction) and a homogeneously illuminated image is used to correct for sensitivity differences between pixels (gain correction). Finally, single pixels and lines with too low or too high signal (“defects”) are corrected by simple interpolation with the neighboring pixels.

The sensor array is produced while the polyimide foil is still attached to a glass carrier. To show that delamination of the foil does not influence the performance of the sensor array, the optical characterization has been done before and after the laser delamination process. The graphs of signal vs. light intensity at two different bias voltages (Fig. 5a) show no difference between the two measurements. We conclude that the delamination process does not affect the sensitivity of the sensor array. In addition, no new defect single pixels, lines or areas with increased dark current were found comparing images before and after releasing the foil from the glass. To prove the long shelf-life, we repeated the same measurement 44 days after the delamination. In between, the sensor array has been kept at ambient air and room temperature. Again, no signs of degradation were found as shown in Fig. 5b. Hence, the bottom and top encapsulation layers, with a water vapor transmission rate WVTR of  $10^{-6}$  g/m<sup>2</sup>/day<sup>19,27</sup>, serve as an excellent barrier for potential degradation by the ambient.

Subsequent to the optical characterization we tested the digital detector also with X-rays. Flexible cesium iodide (CsI) scintillator sheets of 400 and 700  $\mu\text{m}$ , typical thicknesses in current state-of-the-art flat panel X-ray detectors exceeding the attenuation length of 99  $\mu\text{m}$  at the X-ray energy used, were coupled to the sensor array by simply pressing them with the weight of 1 mm Al to

achieve a good optical contact. X-ray images with 70 kV tube voltage and 350 mA tube current were acquired with 50 ms exposure time. No additional filtration other than the internal tube filtration (about 2.5 mm Al equivalent) has been used, i.e., X-ray beam quality is defined as RQR5 with about 40 keV average X-ray energy. With a source-image distance of about 1 m a dose of about 450  $\mu\text{Gy}$  air/frame was applied. Typical X-ray resolution test phantoms with thin lead lamella (Huettnner, type 10) were put as contrast objects on top of the digital detector (Fig. 6).

Similar as with the optical image (Fig. 4d) an offset, gain, and defect correction were performed. The images show a good and homogeneous contrast over the whole area of the digital detector. It is clearly visible that the spatial resolution is higher with the thinner scintillator (Fig. 6a, 400  $\mu\text{m}$ ) layer because the lateral spread of optical photons is lower than in the thicker scintillator layer (Fig. 6b, 700  $\mu\text{m}$ ). The modulation transfer function (MTF), has been measured with a tungsten edge according to IEC standard IEC 62220-1 CDV. It is 31 and 37% at 1 lp/mm for the 700 and 400  $\mu\text{m}$  thick scintillator. These values are in agreement with the expected MTF for an X-ray detector with a 40  $\mu\text{m}$  thin-film barrier in between the image sensor and scintillator (Fig. 2a).

In case of a flat detector, oblique incident X-rays lead to a degradation of the MTF at the edges and corners, because the point of interaction in the layer determines the lateral displacement and leads to a blur. Following the analysis method of Hajdok & Cunningham<sup>28</sup> a MTF degradation of 17% at 2 line pairs per mm is expected. More details can be found in (Fig. S1). By curving the detector with the right radius for a given source-detector distance, all X-rays are impinging perpendicular to the scintillator surface and no degradation due to oblique incident X-ray occurs. The test bench for 3-dimensional X-ray imaging (Fig. 7a) comprises a standard medical X-ray tube (Philips MRC200 0407 ROT-GS 1004), a rotational stage to place objects, and the foil-based digital detector in a curved holder with 32 cm curvature radius. The X-ray beam from the tube passes the object horizontally before hitting the detector. The tube and detector are fixed in their position. The object can be rotated in a controlled manner. This geometry is equivalent to medical CBCT, just in that case the object (patient) is in a fixed position while tube and detector are rotating.

X-ray images of a piece of bone are taken with a rate of 2 images per second while the object is rotating with 4° per second, thus 180 projection images are taken in a full 360° rotation. The steps of offset, gain, and defect correction mentioned earlier were also applied to the 2D projection images. With a standard 3D reconstruction algorithm (FDK filtered back-projection), which has been adapted for the curved geometry, a 3D volume image (Fig. 7b) of  $256 \times 256 \times 256$  voxels with a voxel size of (0.234 mm<sup>3</sup>) is created. Since 3D reconstruction is very sensitive to any nonideal

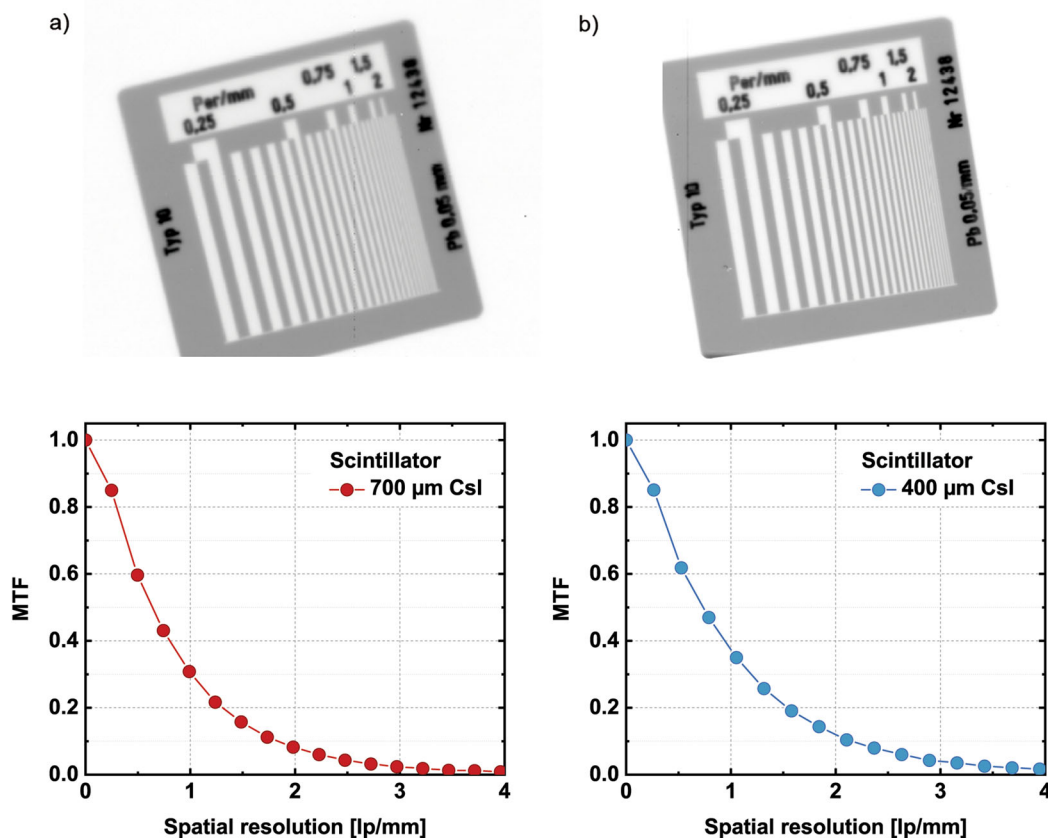


**Fig. 6** 2D X-ray characterization. **a** X-ray images of resolution phantom (Huettnner, type 10, top) and MTF plot (bottom) with CsI scintillator of 400  $\mu\text{m}$  thickness. **b** Same but with CsI scintillator of 700  $\mu\text{m}$  thickness. X-ray settings: 70 kVp, 350 mA tube current, 50 ms exposure time, source-image distance 1 m.

behavior of the digital X-ray detector, our result with the prototype detector is quite remarkable.

## DISCUSSION

Today's flat panel digital X-ray detectors are heavy, difficult to transport, and prone to breakages because they are made on glass substrates. When processed on plastic substrates, such detectors become less vulnerable. Moreover, detectors-on-foil can be mechanically curved. Curving could create a digital X-ray detector that conforms to the specification of different patients. Here, we integrated a curved digital X-ray detector into a demonstration CBCT X-ray system. 3D images of biological objects were taken with a reconstruction algorithm adapted to the curved geometry. The curved digital X-ray detector consisted of solution-processed OPDs on top of an IGZO TFT backplane, on top of a flexible plastic substrate. The prototype digital detector array consists of  $480 \times 640$  pixels with each a size of  $126 \times 126 \mu\text{m}^2$ , thus the X-ray imaging area was  $6.10 \times 8.13 \text{ cm}^2$ . Stability of the digital detector performance could be shown at ambient air conditions for a long time even after delamination of the foil from the support glass substrate. Equipped with a bendable CsI scintillator, the curved digital detector delivered the same X-ray imaging performance as the flat, foil-based digital X-ray detectors. The advantage of this solution is that it can now be built into a much more compact 3D X-ray imaging system with much smaller footprint, as the area for the gantry can shrink by as much as 50%.

## METHODS

### IGZO TFT array

A bottom-gate top-contact TFT layout with an etch-stop layer for the image sensor backplane is used. First, a 150 nm-thick  $\text{SiN}_x$  thin-film moisture barrier was deposited on the top of a 13  $\mu\text{m}$  thick spin-on PI foil applied on a  $320 \times 352 \text{ mm}$  glass plate. A MoCr gate metal was then sputtered and patterned using photolithography, followed by a 200 nm-thick plasma-enhanced chemical vapor deposited (PECVD)  $\text{SiN}_x$  gate dielectric layer deposited at 180 °C. A gate dielectric breakdown field of  $>6 \text{ MV/cm}$  was measured, which is sufficient for the typical voltages used in the TFTs. The semiconductor layer was a 24 nm-thick IGZO layer, deposited using dc sputtering from a target with an In:Ga:Zn atomic ratio of 1:1:1. IGZO layer thickness and  $\text{O}_2$  flow (6%) in the sputter chamber were optimized in order to achieve good TFT performance at low temperature. A 100-nm-thick  $\text{SiO}_2$  etch-stop layer layer was grown using PECVD at 200 °C on top of the patterned IGZO semiconductor. A dry etching process was used to open the contact holes between the gate metal and semiconductor, and finally, source-drain layers, together with interconnect lines, were sputtered from a MoCr target. The TFT stack was encapsulated with a 2  $\mu\text{m}$ -thick photopatternable SU8 resist interlayer. The TFT technology was originally developed to make flexible OLED displays<sup>29</sup>.

### Organic photodetector

A 100 nm of MoCr was sputtered and subsequently patterned using photolithography to form the reflective pixel electrode. Contact holes and the edges of the pixel electrodes were covered with a SU8 resist, preventing shorts between the bottom and the top electrode. The photoactive layer is a 300 nm-thick blend of a p-type polymer, PCDTBT (purchased from PCAS), and n-type small molecule, [6, 6]-phenyl-C61 butyric acid methyl ester (purchased from nano-c) in a 1:4 wt ratio. The bandgap of PCDTBT and PCBM are  $\sim 1.6$  and 2.3 eV, respectively, HOMO  $\sim 5.1$  eV, LUMO  $\sim 3.5$  eV for PCDTBT, HOMO  $\sim 6.1$  eV, and LUMO  $\sim 3.8$  eV for

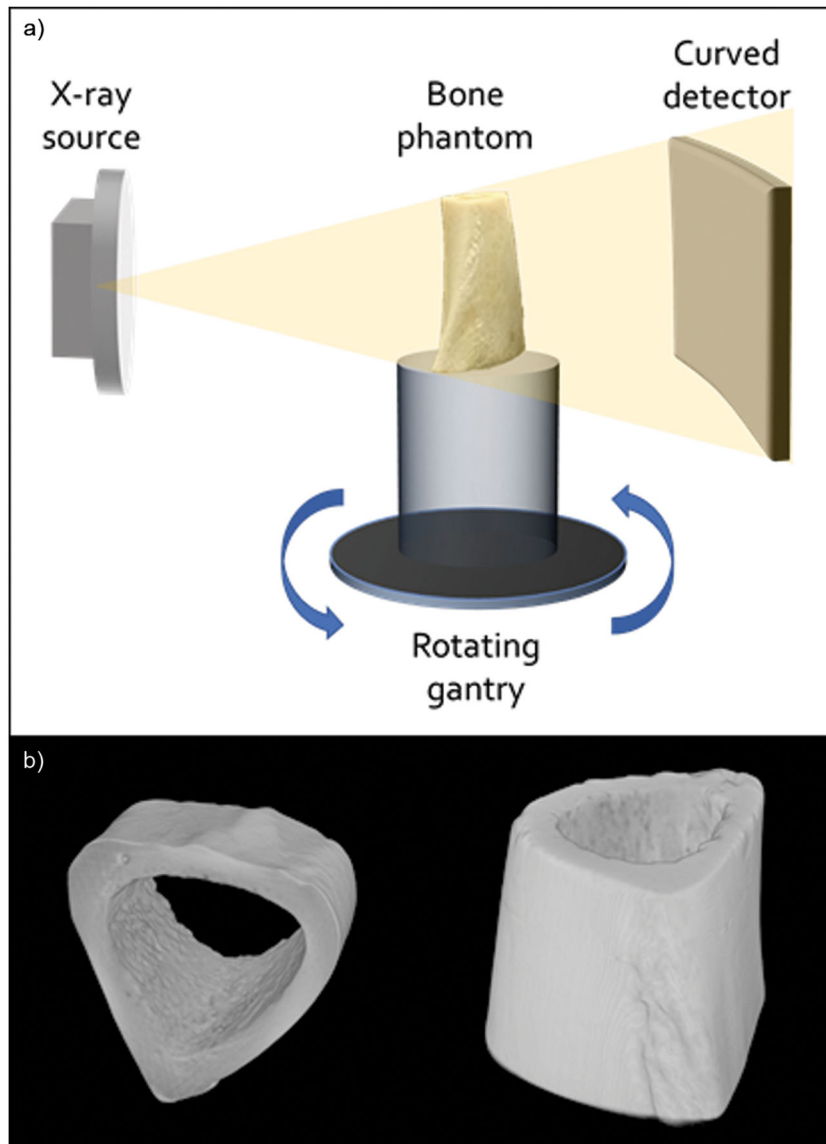


**Fig. 7** 3D X-ray characterization. **a** Schematic of CBCT test bench used for characterization of the curved digital X-ray detector, showing X-ray source, bone phantom, and curved digital X-ray detector. **b** Reconstructed 3D images of the bone phantom.

PCBM. This leads to an optical absorption onset of  $\sim 700$  nm. The photoactive blend was slot die coated from chlorobenzene on top of the TFT backplane. Prior to deposition of the top electrode, the photoactive layer was annealed at 60–90 °C for 10 min in ambient. Thermally evaporated 60 nm  $\text{MoO}_x$  and 10 nm Ag are used as a semitransparent anode. The image sensor on foil was protected from oxygen and moisture by an optically transparent, multi-layer stack of two low-temperature plasma-deposited amorphous hydrogenated silicon nitride ( $a\text{-SiN}_x\text{:H}$ ) layers and an organic intermediate layer<sup>19</sup>. The total thickness of that encapsulation stack is 40  $\mu\text{m}$ .

#### Delamination

In order to release the image sensor on foil from the temporary glass carrier, laser-assisted debonding is used. Three hundred fifty-five nanometers light from 3rd harmonic ND:YAG shines from the backside of the glass carrier onto the polyimide foil. The laser energy has to be able to reach the interface between glass and polyimide. The 3rd harmonic ND:YAG 355 nm is absorbed only slightly by the (Eagle XG) glass carrier, but extremely well by polyimide. In polyimide this laser has a penetration depth of around 50 nm. When the intense laser light is absorbed fully in this very thin polyimide layer, the polyimide foil almost instantaneously

decomposes and gaseous compounds are formed. Heat further pressurizes the gaseous species and triggers delamination of the polyimide foil from the glass. Because of the high absorption of the polyimide, TFT and OPD are screened relatively well from the intense laser light, and therefore the laser does not damage the image sensor during release.

#### Electronic drivers

Each data line is connected to a channel of a charge sensitive amplifier (CSA; type Indigo ISC0701, FLIR systems) with subsequent digitization with 14-bit resolution. The charge of the CSA is sampled with 14 bit, but scaled to 16 bit inside the FPGA of the detector electronics, because all further image processing is done with 16 bit numbers. Gate line drivers from NEC (type uPD160702B) have been used. In the detector mode used, the capacitance of the feedback capacitor of the integrator  $C_{\text{int}}$  equals 4 pF. Additional image corrections such as subtraction of dark images, and correction of individual pixel gain, are done inside the PC, and the resulting image is displayed on the PC monitor.

TFT and OPD characterization: all TFT characteristics were measured in ambient using an Agilent 4155C semiconductor parameter analyzer connected to a semi-automatic prober. OPD test devices were characterized in a glovebox under a  $\text{N}_2$  atmosphere and at ambient temperature.

Current versus voltage characteristics were measured using an Agilent 4155C semiconductor parameter analyzer connected to manual probes. The voltage was swept from  $-2$  to  $2$  V. Using the same equipment, EQE was also measured in a glovebox under a  $N_2$  atmosphere and at ambient temperature. The system uses a solar simulator light source and a series of filters resulting in  $20$ – $50$  nm steps. The devices are connected to a Keithley 2400 to apply the voltage to the devices.

The MTF has been measured with a tungsten edge according to IEC standard IEC 62220-1 CDV.

## DATA AVAILABILITY

The authors declare that the data supporting the findings of this study are available within the paper (and its Supplementary Information files).

Received: 13 November 2019; Accepted: 14 July 2020;

Published online: 09 September 2020

## REFERENCES

- Xu, X., Qi, X., Davanco, M. & Forrest, S. R. Organic photodetector focal plane arrays fabricated on hemispherical substrates by three-dimensional stamping. *LEOS 2007—IEEE Lasers and Electro-Optics Society Annual Meeting Conference Proceedings*, 578 (2007).
- Guenter, B. Highly curved image sensors: a practical approach for improved optical performance. *Opt. Express* **25**, 13010–13023 (2017).
- Dinyari, R., Rim, S. B., Huang, K., Catrysse, P. B. & Peumans, P. Curving monolithic silicon for nonplanar focal plane array applications. *Appl. Phys. Lett.* **92**, 091114 (2008).
- Rim, S.-B., Catrysse, P. B., Dinyari, R., Huang, K. & Peumans, P. The optical advantages of curved focal plane arrays. *Opt. Express* **16**, 4965–4971 (2008).
- Ko, H. C. et al. A hemispherical electronic eye camera based on compressible silicon optoelectronics. *Nature* **454**, 748–753 (2008).
- Lee, W. et al. Two-dimensional materials in functional three-dimensional architectures with applications in photodetection and imaging. *Nat. Commun.* **9**, 1417 (2018).
- Fan, D., Lee, K. & Forrest, S. R. Flexible thin-film InGaAs photodiode focal plane array. *ACS Photonics* **3**, 670–676 (2016).
- Zbijewski, W. et al. A dedicated cone-beam CT system for musculoskeletal extremities imaging: Design, optimization, and initial performance characterization. *Med. Phys.* **38**, 4700–4713 (2011).
- Miracle, A. C. & Mukherji, S. K. Conebeam CT of the head and neck, part 1: physical principles. *Am. J. Neuroradiol.* **30**, 1088–1096 (2009).
- Sisniega, A. et al. Image quality, scatter, and dose in compact CBCT systems with flat and curved detectors. *Proc. SPIE* **10573**, 105734E (2018).
- Gelinck, G. et al. X-ray detector-on-plastic with high sensitivity using low cost, solution-processed organic photodiodes. *IEEE Trans. Electron Devices* **63**, 197–204 (2016).
- Jansen-van Vuuren, R. D., Armin, A., Pandey, A. K., Burn, P. L. & Meredith, P. Organic photodiodes: the future of full color detection and image sensing. *Adv. Mater.* **28**, 4766–4802 (2016).
- Liu, X., Lin, Y., Liao, Y., Wu, J. & Zheng, Y. Recent advances in organic near-infrared photodiodes. *J. Mater. Chem. C* **6**, 3499–3513 (2018).
- García de Arquer, F. P., Armin, A., Meredith, P. & Sargent, E. H. Solution-processed semiconductors for next-generation photodetectors. *Nat. Rev. Mater.* **2**, 16100 (2017).
- Adrien, P. & Ana Claudia, A. Solution-processed image sensors on flexible substrates. *Flex. Print. Electron.* **1**, 043001 (2016).
- Ratcliff, E. L. et al. Energy level alignment in PCDTBT:PC70BM solar cells: Solution processed  $NiO_x$  for improved hole collection and efficiency. *Org. Electron.* **13**, 744–749 (2012).
- Pandey, A. K. et al. Dynamics of charge generation and transport in polymer-fullerene blend elucidated using a photoFET architecture. *ACS Photonics* **1**, 114–120 (2014).
- Yoshida, H. Low-Energy inverse photoemission study on the electron affinities of fullerene derivatives for organic photovoltaic cells. *J. Phys. Chem. C* **118**, 24377 (2014).
- van de Weijer, P. & Akkerman, H. B. Spotless hybrid thin-film encapsulation stack for organic light-emitting diodes on organic foils. *Org. Electron.* **66**, 43–46 (2019).
- Lujan, R. A. & Street, R. A. Flexible X-ray detector array fabricated with oxide thin-film transistors. *IEEE Electron Device Lett.* **33**, 688–690 (2012).
- Ng, T. N. et al. Low temperature a-Si:H photodiodes and flexible image sensor arrays patterned by digital lithography. *Appl. Phys. Lett.* **91**, 063505-1–063505-7 (2007).
- Kielar, M. et al. Long-term stable organic photodetectors with ultra-low dark currents for high detectivity applications. *Sci. Rep.* **6**, 39201 (2016).
- Biele, M. et al. Spray-coated organic photodetectors and image sensors with silicon-like performance. *Adv. Mater. Technol.* **4**, 1800158 (2019).
- Blakesley, J. C. & Speller, R. Modeling the imaging performance of prototype organic X-ray imagers. *Med. Phys.* **35**, 225–239 (2008).
- Overdick, M., Solf, T. & Wischmann, H. A. Temporal artifacts in flat dynamic X-ray detectors. *Proc. SPIE* **4320**, 47–58 (2001).
- Street, R. A. Localized state distribution and its effect on recombination in organic solar cells. *Phys. Rev. B* **84**, 075208 (2011).
- Akkerman, H. B. et al. High-temperature thin-film barriers for foldable AMOLED displays. *J. SID* **26**, 214–222 (2018).
- Hajdok, G. & Cunningham, I. A. Penalty on the detective quantum efficiency from off-axis incident x rays. *Proc. SPIE* **5368**, 109–118 (2004).
- Li, F. et al. Integration of flexible AMOLED Displays using oxide semiconductor TFT backplanes. *SID Symp. Dig.* **45**, 431–435 (2014).

## ACKNOWLEDGEMENTS

The authors would like to thank the process engineers of Holst Center's R&D Pilot Line for the fabrication of the TFT backplanes. Part of the work was financed by the Flexlines project within the Interreg V-program Flanders—The Netherlands, a cross-border cooperation program with financial support from the European Regional Development Fund, and co-financed by the Province of Noord-Brabant, The Netherlands.

## AUTHOR CONTRIBUTIONS

A.v.B., M.S., O.T., J.J., and G.H.G conceived the idea and designed the experiments. A.v.B., M.S., O.T., S.S., J.-L.v.d.S., H.A., A.K., W.R., R.R., L.A., P.E.M., and F.D.R. performed experiments and analyzed the data. A.v.B., M.S., and O.T. coordinated the experiments. J.J. and G.H.G. were project supervisors. A.v.B., M.S., and O.T. wrote the paper, with editing contributions from all the co-authors.

## COMPETING INTERESTS

The authors declare no competing interests.

## ADDITIONAL INFORMATION

**Supplementary information** is available for this paper at <https://doi.org/10.1038/s41528-020-00084-7>.

**Correspondence** and requests for materials should be addressed to G.H.G.

**Reprints and permission information** is available at <http://www.nature.com/reprints>

**Publisher's note** Springer Nature remains neutral with regard to jurisdictional claims in published maps and institutional affiliations.



**Open Access** This article is licensed under a Creative Commons Attribution 4.0 International License, which permits use, sharing, adaptation, distribution and reproduction in any medium or format, as long as you give appropriate credit to the original author(s) and the source, provide a link to the Creative Commons license, and indicate if changes were made. The images or other third party material in this article are included in the article's Creative Commons license, unless indicated otherwise in a credit line to the material. If material is not included in the article's Creative Commons license and your intended use is not permitted by statutory regulation or exceeds the permitted use, you will need to obtain permission directly from the copyright holder. To view a copy of this license, visit <http://creativecommons.org/licenses/by/4.0/>.

© The Author(s) 2020